ARTICLE

Cytotoxicity, anti-microbial studies of M (II)-dithiocarbamate complexes, and molecular docking study against SARS COV2 RNA-dependent RNA polymerase

Ahmed S. M. Al-Janabi[1] 🄸 | Abdulrahman M. Saleh[2] | Mohammad R. Hatshan[3]

[1]Department of Biochemistry, College of Veterinary Medicine, Tikrit University, Tikrit, Iraq

[2]Pharmaceutical Medicinal Chemistry and Drug Design Department, Faculty of Pharmacy, Al-Azhar University, Cairo, Egypt

[3]Department of Chemistry, College of Science, King Saud University, Riyadh, Saudi Arabia

Correspondence
Ahmed S. M. Al-Janabi, Department of Biochemistry, College of Veterinary Medicine, Tikrit University, Tikrit, Iraq.
Email: dr.ahmed.chem@tu.edu.iq

Abstract

Ten transition metal dithiocarbamate (DTC)complexes of the type $[M(\kappa^2\text{-}Et_2DT)_2]$ (**1–5**), and $[M(\kappa^2\text{-}PyDT)_2]$ (**6–10**) (where M = Co, Ni, Cu, Pd, and Pt; Et_2DT = diethyl dithiocarbamate; PyDT = pyrrolidine dithiocarbamate) were synthesized and characterized by different methods. The dithiocarbamate acted as bidentate chelating ligands to afford a tetrahedral complexes with Co(II) ion and square planner with other transition metal ions. The dithiocarbamate complexes showed good activity against the pathogen bacteria species. The results showed the Pt-dithiocarbamate complexes are more active against all the tested bacteria than the Pd-dithiocarbamate complex. The dithiocarbamate complexes displayed the maximum inhibition zone against *E. coli* bacteria, whereas the lowest activity of the dithiocarbamate against *Salmonella typhimurium* bacteria. The cytotoxicity of the Pd(II) and Pt(II) complexes was screened against the MCF-7 breast cancer cell line and the complexes showed moderate activity compared with the *cis*-platin. The results indicated that the MCF7 cells treated with 500 μg\ml of ligands and Pd(II) and Pt(II) complexes after 24 hr exposure showed intercellular space and dead cells. Finally, molecular docking studies were carried out to examine the binding mode of the synthesized compounds against the proposed target; SARS COV2 RNA-dependent RNA polymerase.

KEYWORDS

anti-microbial, cytotoxicity, dithiocarbamate, RNA polymerase, SARS COV2

1 | INTRODUCTION

Metal complexes of dithiocarbamate ligands have been the topic of current and increasing concern because they possess a wide range of medical fields (such as antibacterial, anti-fungal, and anti-inflammatory) and industry, analytical, and organic chemistry.[1–11]

RNA-dependent RNA polymerase (RdRp) is the core enzyme in the replicative cycle of all positive-strand RNA (+RNA) viruses, which catalyzes the replication of RNA from a RNA template.[12–14]

Coronaviruses (order Nidovirales) are a family of +RNA viruses with the largest single-stranded RNA genomes known to date.[15–18] The unusual complex replication and transcription machinery of severe acute respiratory syndrome coronavirus (SARS-CoV) is composed of 16 nonstructural proteins (nsps), produced during co- and post-translational proteolytic processing of two replicase poly-proteins.[17–20]

Studies on the activity of heavy metal chelating factor for their inhibitory effect on the influenza RdRp, reveal both surprising and promising results. Such as the chelating Cu(II) and Zn(II) could, at least theoretically, inhibit the proper folding of RdRpf.[21,22]

Recently a novel SARS-CoV-2 virus properly originated from bat was reported, causes the severe acute respiratory syndrome, known as COVID-19.[23] In this work, we study the effect of the dithiocarbamate complexes with Co(II), Ni(II), Cu(II), Pd(II), and Pt(II) as anti-bacterial against six pathogenic bacteria species (*Staphylococcus aureus*, *Bacillus subtilis*, *Pseudomonas aeruginosa*, *Escherichia coli*, *Salmonella typhimurium*, and *Vibrio Parahemolyticus*) and cytotoxicity of the Pd(II) and, Pt(II) complexes against breast cancer cell line (MCF-7), also, we study the molecular molding their interaction of the prepared complexes with SARS COV2 RNA-dependent RNA polymerase.

2 | RESULTS AND DISCUSSION

2.1 | Synthesis of complexes

The reactions of dithiocarbamate salts {(NaEt$_2$DT) or (NH$_4$) (PyDT)} with NiCl$_2$.6H$_2$O, CoCl$_2$.6H$_2$O, CuCl$_2$.6H$_2$O, K$_2$PdCl$_4$, or K$_2$PtCl$_4$ in 2:1 (ligand: metal) molar ratio, gave complexes of the type [M(κ^2-dithiocarbamate)$_2$] (Scheme 1) in good yield (77–91%). The dithiocarbamate ligands were bonded through the S atoms as bidentate mode.

2.2 | Characterization of complexes

2.2.1 | NMR spectra

The ^{1}H NMR spectra of complexes (**2**, **4**, and **5**) (Figure 1) displayed the protons of Et$_2$DT$^-$ligand as two separated peaks (quartate and triplate) within δH (1.17–1.24) ppm,
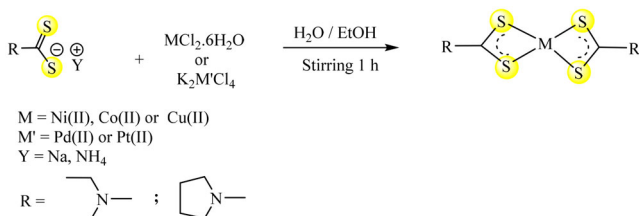
and (3.81–3.85) ppm with coupling constant (6.85–7.92 Hz), due to the methyl and methylene groups, represents **12** protons and **8** protons, respectively.

The ^{1}H NMR spectra of compounds **7**, **9**, and **10** (Figure 2) show the protons of PyDT$^-$ ligand as two multiplet peaks within δH 2.00–2.04 ppm and 3.75–3.76 ppm, assigned to the methylene groups, represent eight protons for each peak, respectively. These results were supported by the ^{13}C NMR spectra of compounds **2**, **4**, **5**, **7**, **9**, and **10**. The ^{13}C NMR spectra of the compounds **2**, **4**, and **5** displayed the chemical shift of the **C**SS-, C^A, and C^B within δH = 200.61–203.63, 12.57–14.30, and 47.59–49.19 ppm, respectively (Figures S1–3), also the ^{13}C NMR spectra of the compounds **2**, **4**, and **5** displayed three peaks at δH = 194.01–195.42, 14.59–15.60, and 44.45–45.71 ppm, due to the chemical shift of the **C**SS-, C^A, and C^B, respectively (Figures S4–6).

2.2.2 | IR spectra

Selected IR bands of the complexes **1–10** are recorded in the experimental part (See Figure 3). In IR spectra which showed two distinguishing bands of dithiocarbamate ligand within 1,487–1,518 and 997–1,024 cm^{-1} refer to the ν(C-N) and ν(CSS) group, respectively. The band of (CSS) group looked as single band without splitting, designated that the dithiocarbamate ligands act as bidentate chelating mode.[24–28] Also the spectra showed frequency of the M-S group at 447–478 cm^{-1}.[24–32]

2.3 | Anti-bacterial activity

The anti-bacterial activity studies of the M(II)-dithiocarbamate complexes are tabulated in Table 1. The results were achieved against six types of the bacteria as the following:

Three as Gram negative bacteria:
- *Staphylococcus aureus*
- *Bacillus subtilis*
- *Pseudomonas aeruginosa*.

Three as Gram positive bacteria:
- *Escherichia coli*
- *Salmonella typhimurium*
- *Vibrio Parahemolyticus*

A standard agar diffusion and broth micro-dilution methods were used, and the results are summarized in
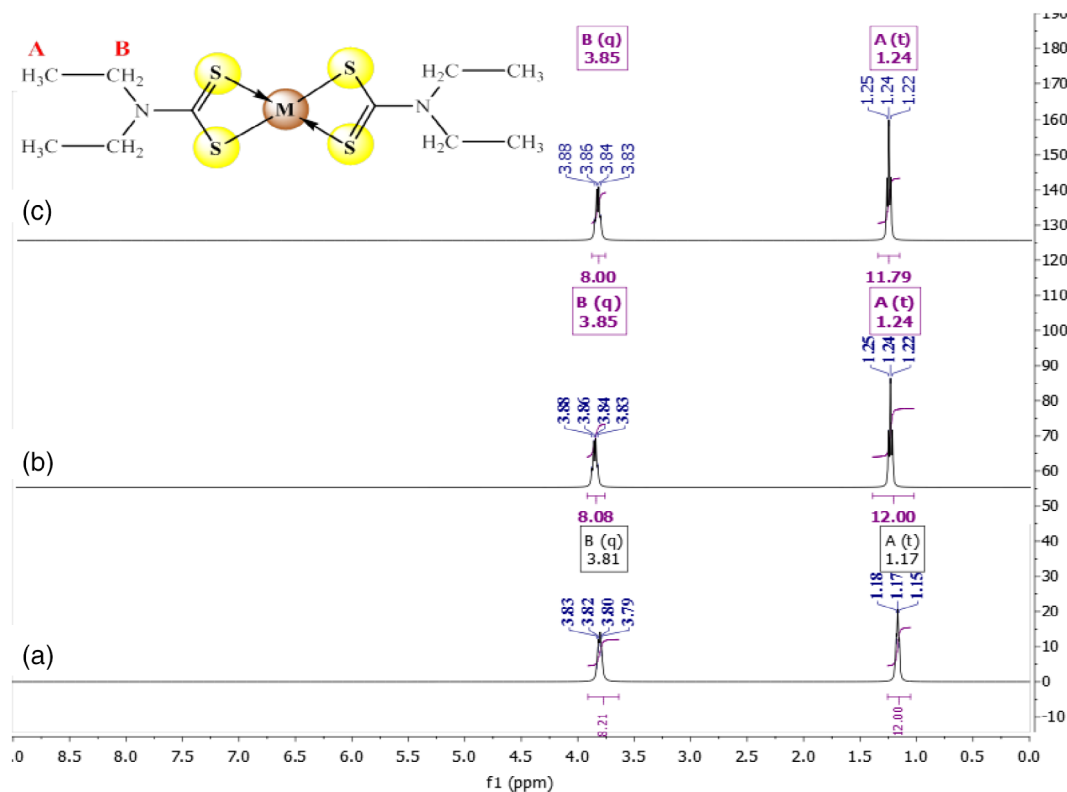

M = Ni(II), Co(II) or Cu(II)
M' = Pd(II) or Pt(II)
Y = Na, NH$_4$

SCHEME 1 Preparation of complex 1–10

FIGURE 1 ^{1}H NMR spectrum of (a) [Ni(κ^2-Et$_2$DT)$_2$] (**2**); (b) [Pd(κ^2-Et$_2$DT)$_2$] (**4**) and (c) [Pt(κ^2-Et$_2$DT)$_2$] (**5**)

Figure 4. The standard error for the test was ±0.03%, and the tests were frequent three periods at similar conditions. The diameter of the inhibitory zone (DIZ) was compared to that of Tetracycline as control positive. The relative (%) activity index was calculated as shown below:

$$\%\text{Activity index} = \frac{\text{Inhibition zone of the test compounds}}{\text{Inhibition zone of the standard drug}} * 100.$$

(1)

The Pd(II) and Pt(II) complexes showed good activity against the pathogen bacteria species. The obtained results can be summarized as following:

1. The Pt(II)-dithiocarbamate complexes are more active against all the tested bacteria then the Pd(II)-dithiocarbamate complexes.
2. [Pt(κ^2-PyDT)$_2$] (**10**) complex showed a highest activity against all tested bacteria compared with other dithiocarbamate complexes.
3. The dithiocarbamate complexes displayed the maximum inhibition zone against *E. coli* bacteria, whereas

the lowest activity of the dithiocarbamate against *Salmonella typhimurium* bacteria.

4. Inhibition order of the complexes are as following:

$$9 > 4 > 5 > 10.$$
Increase of inhibition zone → .

2.4 | Cytotoxicity of Pd(II) and Pt(II) complexes against MCF-7 cell line

The cytotoxicity effect of sodium *N,N*-diethyldithiocarbamate and ammonium pyrrolidine dithiocarbamate against MCF-7 cell line depended on the concentration in time of exposure 24 hr. The maximum inhibitory effect was observed at 500 μg/ml. Therefore, the cytotoxicity of Pd(II) and Pt(II) dithiocarbamate complexes was studied at 500 μg/ml only.

The results of the anti-cancer activity are listed in Table 2. The Pd(II) and Pt(II) complexes show moderate activity compared with the cis-platin. The inhibitory effect against MCF-7 initiated with 23.71% for complex **4** and increased regularly to 23.89% for complex **9**, 40.72%, and 47.76% for the Pt(II) complexes (**5** and **10**) at
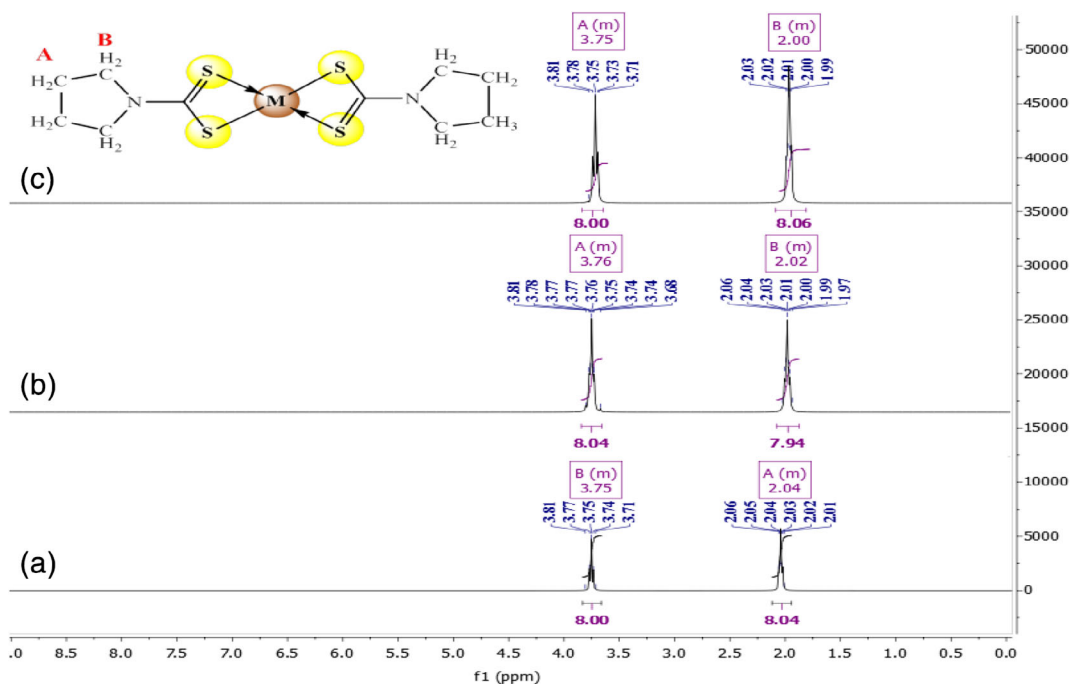
FIGURE 2 ^{1}H NMR spectrum of (a) [Ni(κ^2-PyDT)$_2$] (**7**); (b) [Pd(κ^2-PyDT)$_2$] (**9**); and (c) [Pt(κ^2-PyDT)$_2$] (**10**)
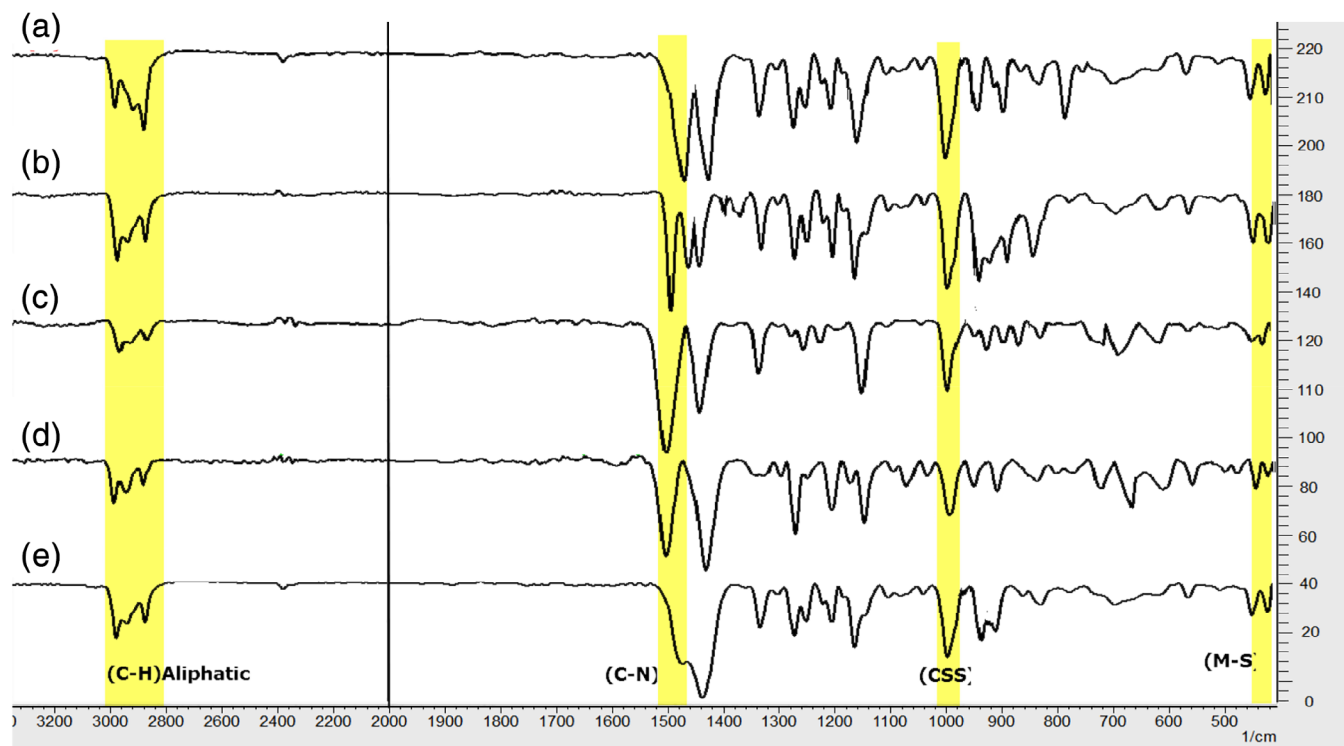

FIGURE 3 IR spectra of complexes (**6–10**)

the same concentration. The results indicated that the MCF7 cells treated with 500 μg/ml of ligands and Pd(II) and Pt(II) complexes after 24 hr exposure showed intercellular space and dead cells as shown in Figures 5 and 6.

2.5 | Molecular docking

The binding mode of the reference (Remdesivir) exhibited an energy binding of −10.56 kcal/mol. By re-docking Remdesivir against SARS COV2 RNA-dependent RNA

TABLE 1 Diameter inhibition zone (mm) and activity index (%) of dithiocarbamate complexes against bacterial species

Compounds	Diameter inhibition zone (mm) (% activity index)					
	P. aeruginosa	*B. Subtills*	*St. aureus*	*E. coli*	*Salmonella typh.*	*Vibrio Parah.*
4	17 (68)	20 (77)	18 (69)	18 (69)	15 (68)	18 (72)
5	21 (76)	23 (88)	20 (77)	22 (85)	17 (77)	22 (88)
9	19 (84)	19 (73)	17 (65)	20 (77)	14 (64)	19 (76)
10	23 (92)	22 (85)	19 (73)	25 (96)	17 (77)	23 (92)
Tetracycline[a]	25 (100)	26 (100)	26 (100)	26 (100)	22 (100)	25 (100)

[a]As positive control, whereas used DMSO as negative control.
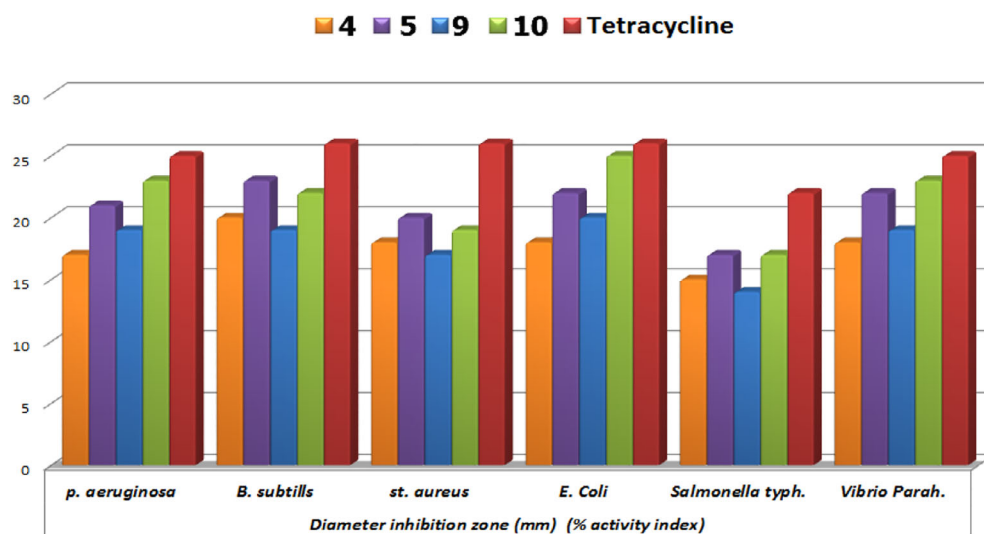
FIGURE 4 Histogram representation of the antibacterial activity of the Pd(II) and Pt(II)

polymerase target site, RMSD value below 2.00 Å (0.6 Å) that means the docking process is valid. From the next figure, amino acids Asp623, Lys621, Cys622, MG1004, and phosphate (pop) 1,003, Asn691, Adenine 11 and Uracil 20 form strong hydrogen bonds with Remdesivir (Figure 7).

The binding mode of the candidate compound **1** exhibited an energy binding of −10.10 kcal/mol. Which a sulfur atoms and Ni metal atom interacted with Asp760, Asp623, Lys621, Cys622, MG1004, phosphate (pop) 1,003 and uracil nucleotide 20 by dipole–dipole and ionic interactions. While the hydrophobic ethyl group formed π-alkyl interactions with adenine nucleotide 11 (Figure 8 (**1**)). Where the binding style of the complex **2** exhibited an energy binding of −5.52 kcal/mol. Which a sulfur atoms and Co metal atom interacted with Val557 and Asp623 by dipole–dipole and ionic π-alkyl interactions. While the hydrophobic ethyl group formed π-alkyl interactions with Cys622, Lys545, Arg555, and adenine nucleotide 19. While sulfur groups formed one hydrogen bonding with adenine nucleotide 11 with distance of 2.90 Å (Figure 8 (**2**)).

The binding mode of the candidate compound **3** exhibited an energy binding of −10.79 kcal/mol. Which a sulfur atoms and Cu metal atom interacted with Asp760, Cys622, MG1004, phosphate (pop) 1,003 and

TABLE 2 Inhibition rate against MCF7 cell line influenced by Pd(II) and Pt(II) complexes after 24 hr exposure (500 μg/ml)

Compound	± SD inhibition rate
NaEt$_2$DT	56.92 ± 6.1
(NH$_4$)(PyDT)	59.83 ± 9.1
[Pd(κ^2-Et$_2$DT)$_2$]	23.89 ± 2.6
[Pt(κ^2-Et$_2$DT)$_2$]	28.93 ± 3.1
[Pd(κ^2-PyDT)$_2$]	29.41 ± 0.9
[Pt(κ^2-PyDT)$_2$]	33.32 ± 8.9

uracil nucleotide 20 by dipole–dipole and ionic π-alkyl interactions. While the hydrophobic ethyl group formed π-alkyl interactions with adenine nucleotide 11, Asn691, and Val 554 (Figure 8 [**3**]). Whereas the complex **4** exhibited an energy binding of −9.50 kcal/mol. Which a sulfur atoms and Pd metal atom interacted with Asp760, Arg555, MG1004, and phosphate (pop) 1,003 by dipole–dipole and ionic π-alkyl interactions. While the hydrophobic ethyl group formed π-alkyl interactions with adenine nucleotide 11, Pro620 and Val 554 (Figure 8 (**4**)).
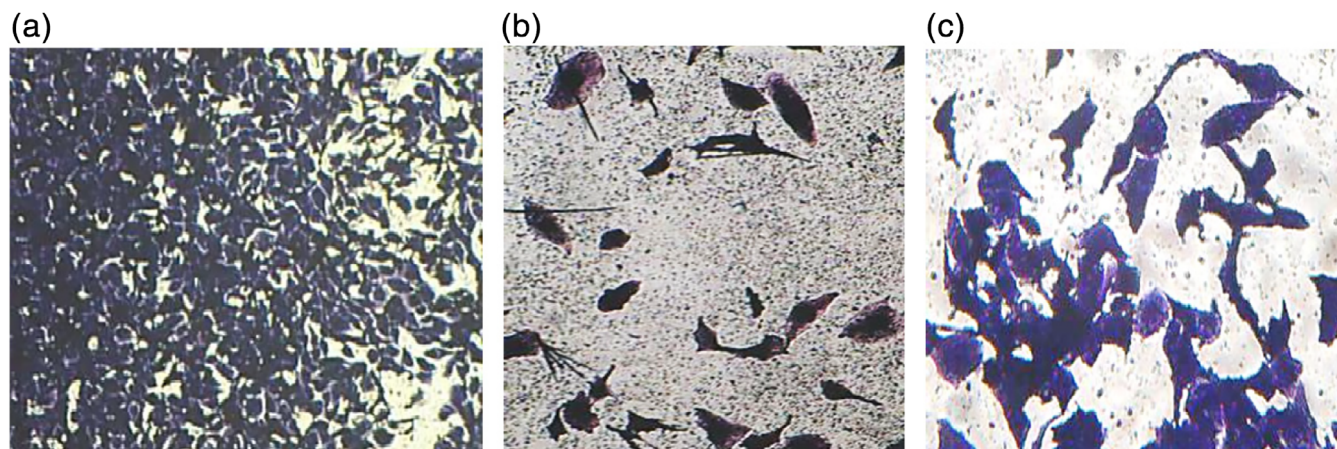
FIGURE 5 (a) Control cancer cells. Apoptotic morphological changes are shown in the cells treated with 500 mg/ml of complexes (b) NaEt$_2$DT (c) (NH$_4$)(PyDT)
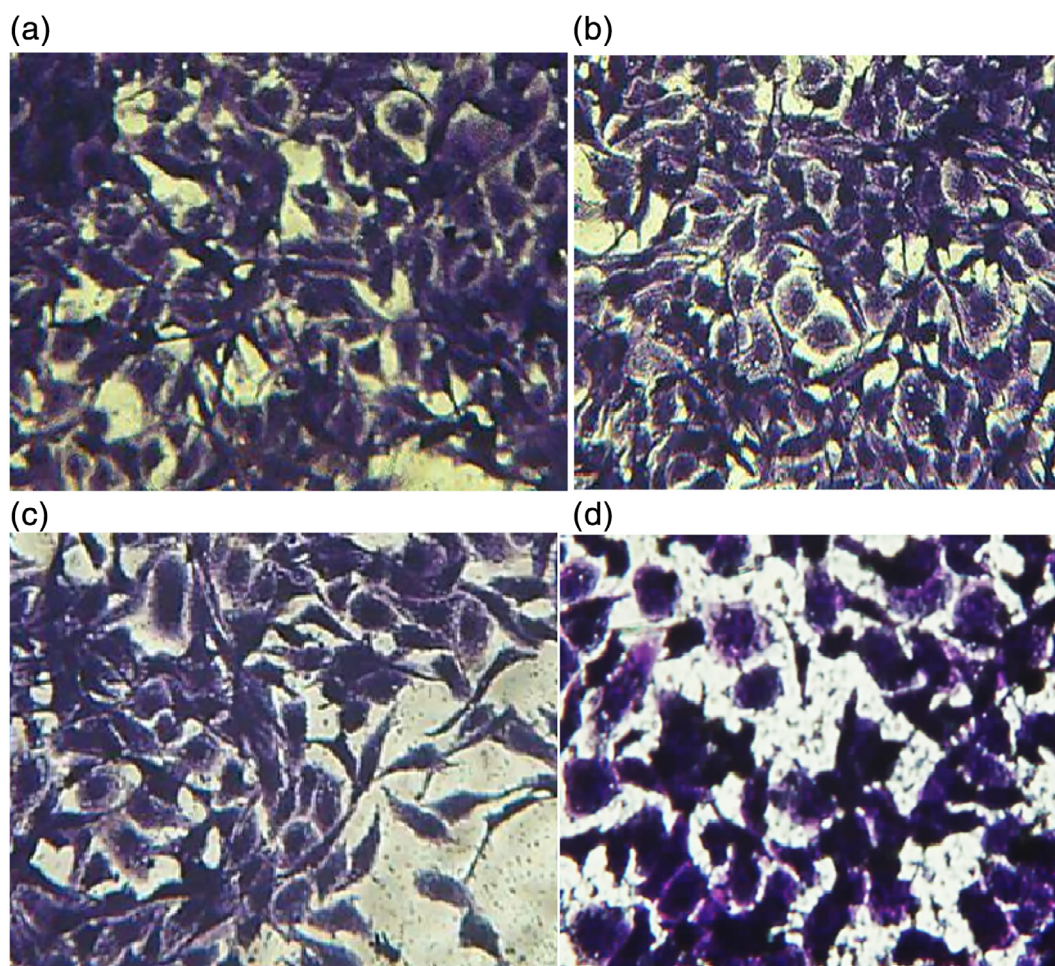

FIGURE 6 Apoptotic morphological changes are shown in the cells treated with 500 mg/ml of complexes (a) [Pd(κ^2-Et$_2$DT)$_2$], (b) [Pd(κ^2-PyT)$_2$] (c) [Pt(κ^2-Et$_2$DT)$_2$] and (d) [Pt(κ^2-PyDT)$_2$] using crystal violet dye

While the complex **5** exhibited an energy binding of −8.89 kcal/mol. Which a sulfur atoms and Pt metal atom interacted with Asp760, Cys622, Asn691, Asp623, Pro20, MG1004 and phosphate (pop) 1,003 by dipole–dipole and ionic interactions. While the hydrophobic ethyl group formed π-alkyl interactions with adenine nucleotide

11, Asn691, and Val 554. The sulfur groups formed one hydrogen bonding with uracil nucleotide 20 with distance of 3.02 Å (Figure 8 (5)).

The binding mode of the candidate complexes 6, 7, and 8 have the same pattern in binding with targeted receptor and exhibited an energy binding of −9.33, −9.37, and −5.51 kcal/mol, respectively. Which a sulfur atoms and Ni, Co and Cu metal atoms interacted with Asp760,

Asp623, Arg555, Lys621, Lys551, Asp761, Ser814, MG1004, phosphate (pop) 1,003 and uracil 20 by dipole–dipole and ionic interactions. (Figure 9 (1–3)).

The binding mode of the candidate compound 9 exhibited an energy binding of −7.93 kcal/mol. Which a sulfur atoms and Pd metal atom interacted with Asp760, Cys622, Asp623, MG1004, phosphate (pop) 1,003, adenine nucleotide 11 and uracil nucleotide 20 by dipole–dipole and ionic interactions. While the pyrrolidine ring formed π-alkyl interaction with Ala558. The sulfur groups formed one hydrogen bonding Asp760 with distance of 2.65 Å (Figure 9 (4)).

The binding mode of the candidate compound 10 exhibited an energy binding of −8.53 kcal/mol). Which a sulfur atoms and Pt metal atoms interacted with Asp760, Arg555, Lys551, Asp761, Ser814, MG1004, phosphate (pop) 1,003, and uracil 20 by dipole–dipole and ionic interactions. The SH group formed one hydrogen bonding Asp761 with distance of 2.85 Å (Figure 9 (5)).

Molecular mapping surface was done to expect how the candidate occupying the critical targeted pocket. Compounds 1, 3, 4 and 7 are showing good occupying the critical space inside the target protein (Figure 10).
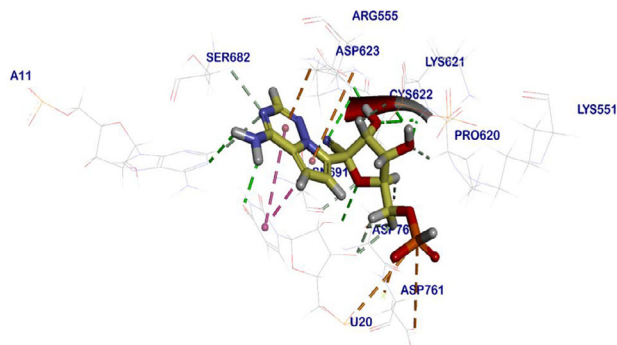

FIGURE 7 Remdesivir *docked in* SARS COV2 RNA-dependent RNA polymerase, charged interaction brown, hydrogen bonds (green) and the π interactions are represented in purple lines

FIGURE 8 Complexes **1–5** docked in SARS COV2 RNA-dependent RNA polymerase, charged interaction brown, hydrogen bonds (green) and the πinteractions are represented in purple lines

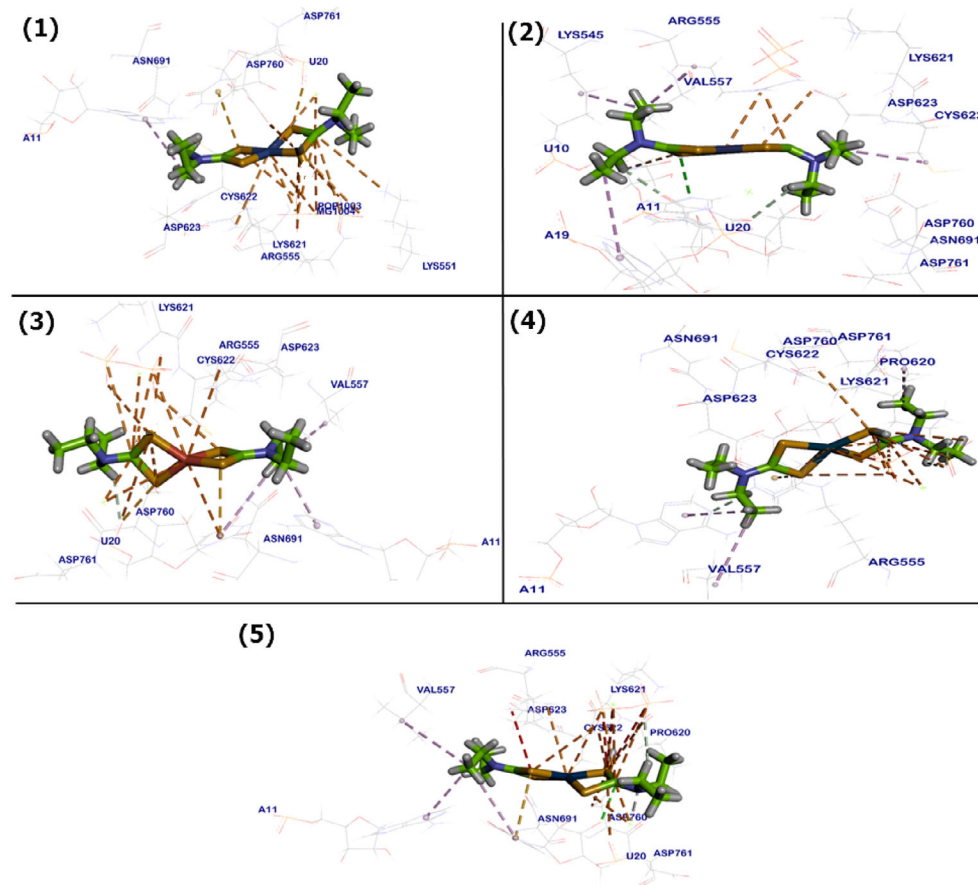**FIGURE 9** Complexes **6–10** docked in SARS COV2 RNA-dependent RNA polymerase, charged interaction brown, hydrogen bonds (green) and the π interactions are represented in purple lines
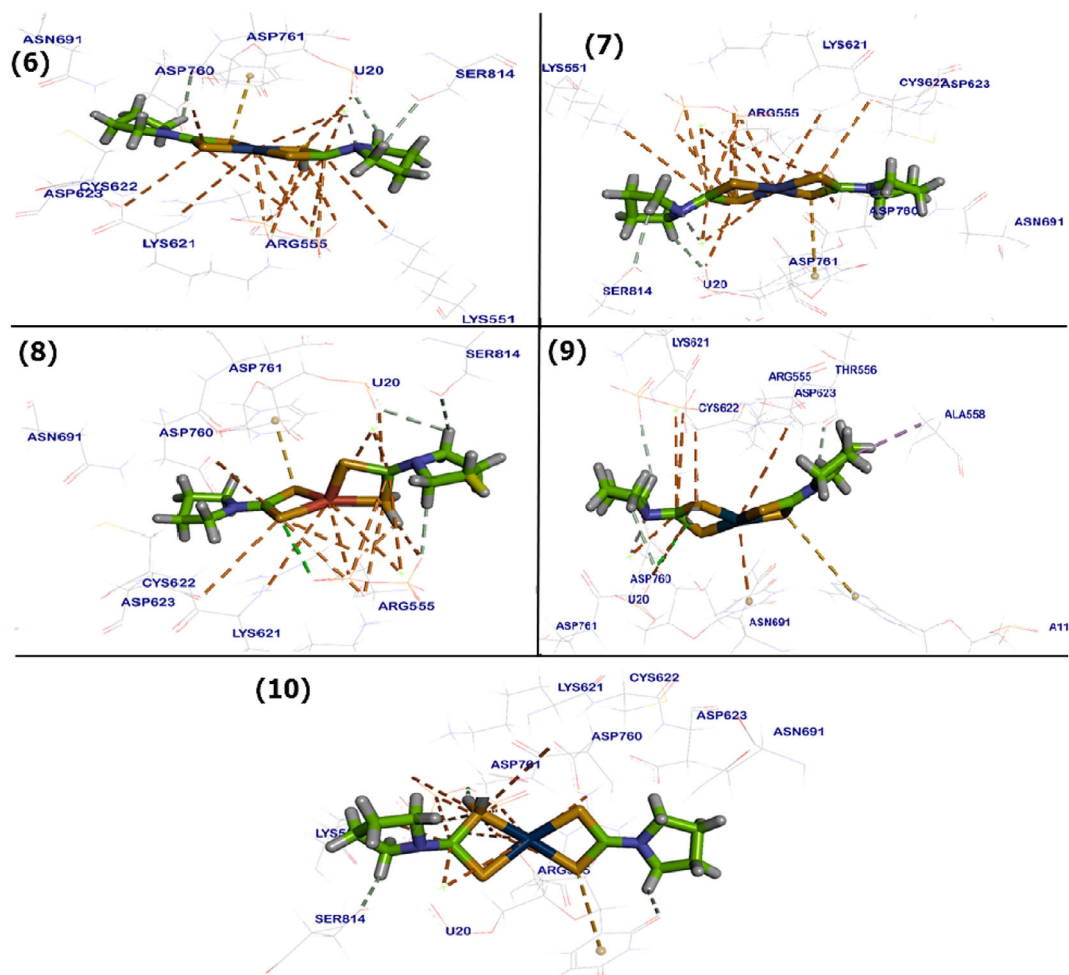
3 | EXPERIMENTAL

3.1 | Materials and methods

All materials {NaEt$_2$DT = diethyl dithiocarbamate; (NH$_4$)(PyDT) = pyrrolidine dithiocarbamate NiCl$_2$.6H$_2$O, CoCl$_2$.6H$_2$O, CuCl$_2$.6H$_2$O, K$_2$PdCl$_4$ or K$_2$PtCl$_4$) and solvents were supplied from Sigma Aldrich or Alfa-Aser and used without further purification. IR spectra were measured by Shimadzu model FTIR-8400S instrument. Elemental analysis (CHN), molar electric conductivity, and melting point were recorded on Euro-vector model EA 3000, digital conductivity meter model CD-2005, and Stuart model SMP10, respectively.

3.2 | Preparation of [co(κ²-Et$_2$DT)$_2$] (1)

An aqueous solution of sodium *N,N*-diethyldithiocarbamate NaEt$_2$DT (0.500 g, 2.92 mmol) (10 ml) was added to an aqueous solution of cobalt chloride (0.347 g, 1.46 mmol)

(15 ml). A dark violet ppt. was formed directly. The mixture was stirred for 1 hr at room temperature, then filtered off, washed with ethanol, and dried under vacuum (Yield: 79%, Melting point(°C): 287–289 (Decompose)).

The following complexes [Ni(κ²-Et$_2$DT)$_2$] (**2**), [Cu(κ²-Et$_2$DT)$_2$] (**3**), [Pd(κ²-Et$_2$DT)$_2$] (**4**), [Pt(κ²-Et$_2$DT)$_2$] (**5**), [Co(κ²-PyDT)$_2$] (**6**), [Ni(κ²-PyDT)$_2$] (**7**), [Cu(κ²-PyDT)$_2$] (**8**), [Pd(κ²-PyDT)$_2$] (**9**) and [Pt(κ²-PyDT)$_2$] (**10**) were prepared and isolated using similar methods.

[Co(κ²-Et$_2$DT)$_2$] (**1**) Dark violet solid. Yield: 79%. Anal. calc. For C$_{10}$H$_{20}$CoN$_2$S$_4$: C, 33.79; H, 5.67; N, 7.88; S, 36.08. Found: C, 34.07; H, 5.93; N, 8.12; S, 36.21%. Molar conductivity in DMF: 11.4 (Ω^{-1} cm^{-1} mol^{-1}). IR (KBr) 2,974 m, 2,869 w, 1,502 s, 1,437 s, 995 m, 563 m, 449w cm^{-1}. Melting point: 287–289°C (Decompose).

[Ni(κ²-Et$_2$DT)$_2$] (**2**) Pale green solid. Yield: 87%. Anal. calc. For C$_{10}$H$_{20}$PdN$_2$S$_4$: C, 29.81; H, 5.00; N, 6.95; S, 31.83. Found: C, 30.05; H, 5.16; N, 7.23; S, 31.97%. Molar conductivity in DMF: 11.4 (Ω^{-1} cm^{-1} mol^{-1}). IR (KBr) 2,955 w, 2,856 m, 1,504 s, 1,441 s, 1,012 m, 576 m, 495w cm^{-1}. ^{1}H NMR (DMSO-*d$_6$*): δ 1.24 (*t*, J_{HH} = 7.80 Hz, 12H,
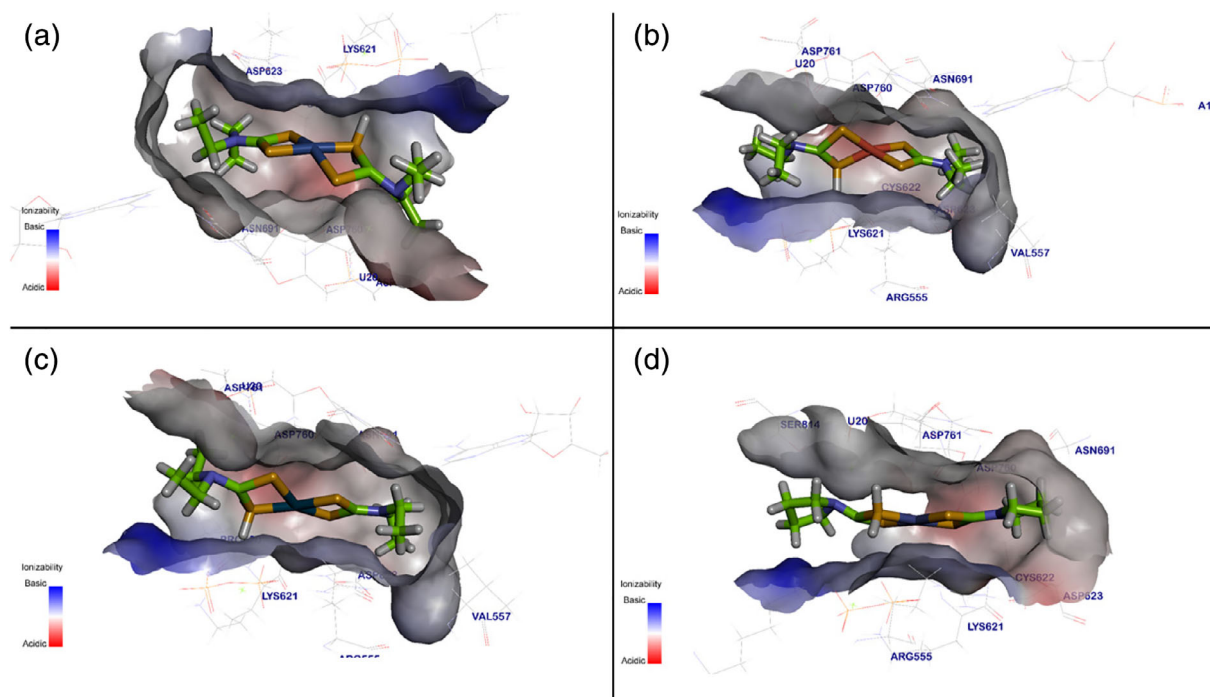
FIGURE 10 Mapping surface showing compounds **1**, **3**, **4**, and **7** occupying the active pocket of SARS COV2 RNA-dependent RNA polymerase. (a) [Co(k2-Et2DT)2](1) (b) [Cu(k2-Et2DT)2](3) (c) [Pd(k2-Et2DT)2](4) and (d) [Ni(k2-PyDT)2](7)

4CH$_3$); 3.85(q, J_{HH} = 7.80 Hz, 8H, 4CH$_2$) ppm. ^{13}C NMR (DMSO-d_6): δ 200.61(**C**SS); 48.88 (**C**H$_2$); 12.57 (**C**H$_3$) ppm. Melting point: 157–160°C (Decompose).

[Cu(κ^2-Et$_2$DT)$_2$] (**3**) Brown-green solid. Yield: 96%. Anal. calc. For C$_{10}$H$_{20}$CuN$_2$S$_4$: C, 33.36; H, 5.60; N, 7.78; S, 35.62. Found: C, 33.27; H, 5.43; N, 7.92; S, 35.45%. Molar conductivity in DMF: 7.30 (Ω^{-1} cm^{-1} mol^{-1}). IR (KBr) 2,893 m, 2,842 w, 1,523 s, 1,427 s, 1,002 m, 554 m, 489w cm^{-1}. Melting point: 291–293°C (Decompose).

[Pd(κ^2-Et$_2$DT)$_2$] (**4**) Brownish yellow solid. Yield: 91%. Anal. calc. For C$_{10}$H$_{20}$PdN$_2$S$_4$: C, 29.81; H, 5.00; N, 6.95; S, 31.83. Found: C, 30.05; H, 5.16; N, 7.23; S, 31.97%. Molar conductivity in DMF: 6.11 (Ω^{-1} cm^{-1} mol^{-1}). IR (KBr) 2,955 w, 2,856 m, 1,504 s, 1,441 s, 1,012 m, 576 m, 495w cm^{-1}. ^{1}H NMR (DMSO-d_6): δ 1.24 (t, J_{HH} = 7.63 Hz, 12H, 4CH$_3$); 3.85 (q, J_{HH} = 7.60 Hz, 8H, 4CH$_2$) ppm. ^{13}C NMR (DMSO-d_6): δ 203.62(**C**SS); 49.19 (**C**H$_2$); 12.81(**C**H$_3$) ppm. Melting point: 157–160°C (Decompose).

[Pt(κ^2-Et$_2$DT)$_2$](**5**) Brownish yellow solid. Yield: 82%. Anal. calc. For C$_{10}$H$_{20}$PtN$_2$S$_4$: C, 24.43; H, 4.10; N, 5.70; S, 26.09. Found: C, 24.61; H, 4.29; N, 5.81; S, 26.32%. Molar conductivity in DMF: 9.76 (Ω^{-1} cm^{-1} mol^{-1}). IR (KBr) 2,948 w, 2,877 m, 1,522 s, 1,438 s, 1,007 m, 521 m, 476w cm^{-1}. ^{1}H NMR (DMSO-d_6): δ 1.17 (t, J_{HH} = 8.00 Hz, 12H, 4CH$_3$); 3.85 (q, J_{HH} = 8.00 Hz, 8H,

TABLE 3 ΔG (kcal/mol) of tested candidates against (SARS COV2 RNA-dependent RNA polymerase) target site PDB ID: 7BV2

Complexes	Score (ΔG)	RMSD value
1	−10.10	1.95
2	−5.52	1.99
3	−10.79	1.23
4	−9.50	1.84
5	−8.89	0.83
6	−9.33	1.59
7	−9.37	0.99
8	−5.51	1.09
9	−7.93	1.75
10	−8.53	1.57
Remdesivir	−10.56	0.6

Note: ΔG = binding free energy.
Abbreviations: RMSD, root-mean-square deviation.

4CH$_2$) ppm. ^{13}C NMR (DMSO-d_6): δ 201.26 (**C**SS); 47.59 (**C**H$_2$); 14.30(**C**H$_3$) ppm. Melting point: 157–160°C (Decompose).

[Co(κ^2-PyDT)$_2$] (**6**) Violet solid. Yield: 81%. Anal. calc. For C$_{10}$H$_{16}$Co$_2$S$_4$: C, 34.18; H, 4.59; N, 7.97; S, 36.49. Found: C, 34.26; H, 4.71; N, 8.25; S, 36.61%. Molar conductivity in DMF: 8.90 (Ω^{-1} cm^{-1} mol^{-1}). IR (KBr)

2,934w, 2,856 m, 1,497 s, 1,451 s, 1,006 m, 561 m, 469w cm^{-1}. Melting point: 256–257°C (Decompose).

[Ni(κ^2-PyDT)$_2$] (**7**). Yellowish blue. Yield: 86%. Anal. calc. For C$_{10}$H$_{16}$NiN$_2$S$_4$: C, 34.20; H, 4.59; N, 7.98; S, 36.52. Found: C, 34.42; H, 4.81; N, 8.07; S, 36.39%. Molar conductivity in DMF: 8.71 (Ω^{-1} cm^{-1} mol^{-1}). IR (KBr) 2,974 w, 2,834 w, 1,517 s, 1,434 s, 1,006 s, 571 s, 456 w cm^{-1}. δ ^{1}H NMR (DMSO-d_6): δ 2.04 (m, 8H, 4CH$_2$^{B}); 3.75 (m, 8H, 4CH$_2$^{A}) ppm. ^{13}C NMR (DMSO-d_6): δ195.42 (**C**SS); 45.33 (**C**H$_2$^{B}); 14.72 (**C**H$_2$^{A}) ppm. Melting point: 231-233°C (Decompose).

[Cu(κ^2-PyDT)$_2$] (**8**). Green-blue solid. Yield: 78%. Anal. calc. For C$_{36}$H$_{40}$CuN$_2$P$_2$S$_4$: C, 33.74; H, 4.53; N, 7.87; S, 36.02. Found: C, 33.63; H, 4.77; N, 7.98; S, 36.14%. Molar conductivity in DMF: 5.40 (Ω^{-1} cm^{-1} mol^{-1}). IR (KBr) 2,891 w, 2,828 w, 1,543 s, 1,441 s, 1,034 m, 545 s, 504 w cm^{-1}. Melting point: 312-314°C (decompose)..

[Pd(κ^2-PyDT)$_2$] (**9**). Yellow solid. Yield: 83%. Anal. calc. For C$_{10}$H$_{16}$PdN$_2$S$_4$: C, 30.11; H, 4.04; N, 7.02; S, 32.15. Found: C, 30.02; H, 4.23; N, 7.17; S, 32.29%. Molar conductivity in DMF: 4.78 (Ω^{-1} cm^{-1} mol^{-1}). IR (KBr) 2,974 w, 2,826 w, 1,523 s, 1,435 s, 989 s, 526 s, 435w cm^{-1}. δ ^{1}H NMR (DMSO-d_6): δ 2.02 (m, 8H, 4CH$_2$^{B}); 3.76 (m, 8H, 4CH$_2$^{A}) ppm. ^{13}C NMR (DMSO-d_6): δ 193.39(**C**SS); 45.71 (**C**H$_2$^{B}); 15.60 (**C**H$_2$^{A}) ppm Melting point: 134-136°C.

[Pt(κ^2-PyDT)$_2$] (**10**) Orange-yellow. Yield: 77%. Anal. calc. For C$_{10}$H$_{16}$PtN$_2$S$_4$: C, 24.63; H, 3.31; N, 5.75; S, 26.30. Found: C, 24.83; H, 3.49; N, 5.92; S, 26.19%. Molar conductivity in DMF: 6.76 (Ω^{-1} cm^{-1} mol^{-1}). IR (KBr) 2,948 w, 2,877 m, 1,496 s, 1,456 s, 1,012 m, 462 s cm^{-1}. ^{1}H NMR (DMSO-d_6): δ 2.00 (m, 8H, 4CH$_2$^{B}); 3.75 (m, 8H, 4CH$_2$^{A}) ppm. ^{13}C NMR (DMSO-d_6): δ 194.59 (**C**SS); 44.54 (**C**H$_2$^{B}); 14.59 (**C**H$_2$^{A}) ppm Melting point: 168–170°C (Decompose) .

3.3 | Antibacterial studies

The antibacterial activity of the Pd(II) and Pt(II)-dithiocarbamate complexes was examined against six pathogenic bacteria, *Staphylococcus aureus*, *Bacillus subtilis*, *Pseudomonas aeruginosa*, *Escherichia coli*, *Salmonella typhimurium*, and *Vibrio Parahemolyticus*. in DMSO as a solvent at 1×10^{-3} M concentration. The activity of the Pd(II) and Pt(II) complexes was tested by agar disc diffusion method designated by Molder et al.[33] and the results were compared with *Tetracycline* as standard antibiotic.

3.4 | Cytotoxicity studies

The cytotoxicity of Pd(II) and Pt(II)complexes was screened against MCF7 breast cancer cell line by adding

trypsin-version solution to the tissue culture flask (size 25 cm^2), then 20 ml of the RPMI-1640 medium was added with fetal calf serum (FCS). The cells were mixed and 0.2 ml was transferred from each mixture into each of the 96 wells using a fine automatic pipette. The plates were left in the incubator at 37°C for 18–24 hr until the adhesion of cells in the well, then the old media from wells were removed, 0.2 ml of the prepared concentrations of dithiocarbamate ligands were added using the Serum-free media (15.1, 31.2, 62.5, 125, 250, 400, and 500 μg/ml) with three replicates per a concentration. In addition, 0.2 ml of the prepared concentrations of each complexes were added using the Serum-free media (500 μg/ml) only. Four replicates were performed using DMSO (dimethyl sulfoxide) as a negative control and four replicates were added to PBS supplemented with 0.2 ml of serum free medium assay positive control and plates were incubated at 37°C for 24 hr according to the method mentioned. The plate was taken out from the incubator and 50 μl of crystal violet stain per well was added then returned to the incubator for 20 min. After that, the contents were removed and washed with PBS until the excess dye was removed and the cells were allowed to dry. The results were read using the optical spectroscopy device at a wave length of 492 nm. The rate was determined to inhibit the growth of cancer cells according to the following equation:

$$\text{Inhibition rate (IR)}\% = (A - B \backslash A) \times 100, \qquad (2)$$

where A is the control reading and B is the treatment reading for each concentration.

3.5 | Molecular docking studies

Docking study was applied to identify the possible binding interactions between the active candidates and SARS COV2 RNA-dependent RNA polymerase-targeted site. Docking study will provide some insights into the additional structural alterations and development of new more potent and selective SARS COV2 RNA-dependent RNA polymerase inhibitors. In the present research, a molecular modeling study which relied on SARS COV2 RNA-dependent RNA polymerase crystal structure (PDB code 7BV2) was executed applying "molecular operating environment (MOE) version 2019.01" Chemical Computing Group Inc. software.[34] At first, water molecules have been removed from the complex. Then, crystallographic disorders and unfilled valence atoms were corrected using protein report and utility and clean protein options. Protein energy was minimized by applying MMFF94 force fields. The rigid of binding Site was structure of

protein was obtained by applying fixed atom constraint. The protein essential amino acids were defined and prepared for docking process. Two-dimensional structures of tested compounds were drawn using Chemo-Bio Draw Ultra16.0 and saved in MDL-SD file format, from MOE 19.012 software, the saved file was opened, 3D structures were protonated and energy was minimized by applying.05 RMSD kcal/mol. MMFF94 force field. Then, the minimized structures were prepared for docking using prepared ligand protocol. Molecular docking process was carried out using the CDOCKER protocol. The receptor was held rigid while the ligands were allowed to be flexible during the refinement each molecule was allowed to produce 10 different interaction poses with the protein. Then docking scores (-CDOCKER interaction energy) of the best-fitted poses with the active site at SARS COV2 RNA-dependent RNA polymerase was recorded and 3D view was generated by Discovery Studio 2016 Client software. We use all these processes to predict the proposed binding mode, affinity, preferred orientation of each docking pose, and binding free energy (ΔG) of the tested compounds with SARS COV2 RNA-dependent RNA polymerase and the binding free energy (ΔG) of the tested compounds are listed in Table 3.

3.5.1 | Active site prediction

The active site was predicted by using the site finder option of using MOE 19.01 software.[34] The site finder option was used to calculate possible active sites in SARS COV2 RNA-dependent RNA polymerase. Calculations were made to determine potential sites for ligand binding and docking, and restriction sets for rendering partial molecular surfaces. *In* SARS COV2 RNA-dependent RNA polymerase *critical active site contain* Asp623, Lys621, Cys622, Asp760, MG1004, and phosphate (pop) 1,003, Asn691, adenine 11 and uracil 20 *amino acid and nucleotides residues*.

4 | CONCLUSIONS

Transition metal dithiocarbamate complexes of the type [M(κ^2-Et$_2$DT)$_2$] (**1–5**), and [M(κ^2-PyDT)$_2$] (**6–10**) (M = Co, Ni, Cu, Pd and Pt) have been synthesized and characterized by different techniques. The DTC ligands are coordinated as bidentate chelating ligand through the sulfur atom of the CSS group. The dithiocarbamate complexes showed good activity against the tested bacteria species, and displayed the maximum inhibition zone against *E. coli* bacteria, whereas the lowest activity

against *Salmonella typhimurium* bacteria, and the inhibition order of the DTC complexes are as following:

$$9 > 4 > 5 > 10.$$

Increase of inhibition zone $\rightarrow$.

The cytotoxicity of the Pd(II) and Pt(II) complexes was screened against MCF-7 breast cancer cell line. The inhibitory effect against MCF-7 which initiated with 23.71% for (**4**) and increased regularly to 23.89% for complex (**9**), 40.72% and 47.76% for the Pt(II) complexes (**5** and **10**) at the same concentration. Additionally, the tested compounds showed promising activities against SARS COV2 RNA-dependent RNA polymerase, in which the most of candidates have a good binding mode and excellent interaction with critical amino acids in targeted pocket, moreover candidate **1, 3, 4**, and **7** have the score-**10.10, −10.79, −9.50**, and − **9.37**, respectively, which compared with remdesivir −10.56, compound **3** may be better than remdesivir.

ORCID
Ahmed S. M. Al-Janabi https://orcid.org/0000-0003-2722-7419

REFERENCES
[1] G. Hogarth, *Mini-Rev. Med. Chem.* **2012**, *12*, 1202. https://doi.org/10.2174/138955712802762095.

[2] M. K. Amir, S. Z. Khan, F. Hayat, A. Hassan, I. S. Butler, Zia-ur-Rehman, *Inorg. Chim. Acta* **2016**, *451*, 31. https://doi.org/10.1016/j.ica.2016.06.036.

[3] A. T. Odularu, P. A. Ajibade, *Bioinorg. Chem. Appl.* **2019**, *2019*, 1. https://doi.org/10.1155/2019/8260496.

[4] J. W. d. F. Oliveira, H. A. O. Rocha, W. M. T. Q. de Medeiros, M. S. Silva, *Molecules* **2019**, *24*, 2806. https://doi.org/10.3390/molecules24152806.

[5] I. Haiduc, *Compr. Coord. Chem. II* **2004**, *1*, 349. https://doi.org/10.1016/B0-08-043748-6/01121-X.

[6] P. J. Heard, in *Progress in Inorganic Chemistry*, Vol. 53 (Ed: K. D. Karlin) John Wiley & Sons, Inc, Hoboken, NJ **2005**, p. 1. https://doi.org/10.1002/0471725587.ch1.

[7] G. Hogarth, in *Progress in Inorganic Chemistry*, Vol. 53 (Ed: K. D. Karlin) John Wiley & Sons, Inc., Hoboken, NJ **2005**, p. 71. https://doi.org/10.1002/0471725587.ch2.

[8] N. Shimar, Z. Goh, Y. Kqueen, K. Ang, J. Horng, C. Hoon, Z. Abidin, S. Nadiah, B. Abdul, S. Weng, H. Seng, E. R. T.

Tiekink, *Eur. J. Med. Chem.* **2013**, *67*, 127. https://doi.org/10.1016/j.ejmech.2013.06.038.

[9] A. I. A. Al-Nassiry, A. S. M. Al-Janabi, O. Y. T. Al-Janabi, P. Spearman, M. A. Al-Heety, *J. Chin. Chem. Soc.* **2020**, *67*, 775. https://doi.org/10.1002/jccs.201900349.

[10] A. S. M. Al-Janabi, O. A. Y. Al-Samrai, T. A. Yousef, *Appl. Organomet. Chem.* **2020**, *34*, e5967. https://doi.org/10.1002/aoc.5967.

[11] M. M. Salman, A. A. Al-Dulaimi, A. S. M. Al-Janabi, M. A. Al-Heety, *Mater. Today: Proc.* **2020**. https://doi.org/10.1016/j.matpr.2020.07.082.

[12] B. M. Krenn, E. Gaudernak, B. Holzer, K. Lanke, F. J. M. Van Kuppeveld, *Infections. J. Virol.* **2009**, *83*, 58.

[13] P. D. Zalewski, I. J. Forbes, W. H. Betts, *Biochem. J.* **1993**, *296*, 403.

[14] M. Hung, C. S. Gibbs, *Antiviral Res.* **2002**, *56*, 99.

[15] A. E. Gorbalenya, L. Enjuanes, J. Ziebuhr, *E. J. Virus Res.* **2006**, *117*, 17.

[16] S. Perlman, J. Netland, *Nat. Rev. Microbiol.* **2009**, *7*, 439.

[17] M. J. van Hemert, S. H. van den Worm, K. Knoops, A. M. Mommaas, A. E. Gorbalenya, *PLoS Pathog* **2008**, *4*, e1000054.

[18] A. J. te Velthuis, J. J. Arnold, C. E. Cameron, S. H. van den Worm, E. J. Snijder, *Nucleic Acids Res.* **2009**, *38*, 203.

[19] A. C. Sims, S. E. Burkett, B. Yount, R. J. Pickles, *Virus Res.* **2008**, *133*, 33.

[20] L. J. Stockman, R. Bellamy, P. Garner, *PLoS Med.* **2006**, *3*, e343.

[21] K. E. Prosser, A. W. Y. Leung, S. Harrypersad, A. R. Lewis, M. B. Bally, C. J. Walsby, *Chem. A Eur. J.* **2018**, *24*, 6334. https://doi.org/10.1002/chem.201800289.

[22] a) U. C. Chaturvedi, R. Shrivastava, *FEMS Immunol. Med. Microbiol.* **2005**, *43*(2), 105. https://doi.org/10.1016/j.femsim.2004.11.004. b) A. J. W. te Velthuis, S. H. E. van den Worm, A. C. Sims, R. S. Baric, E. J. Snijder, M. J. van Hemert, *PLoS Pathog* **2011**, *6*, e1001176.

[23] a) D. Chang, M. Lin, L. Wei, L. Xie, G. Zhu, C. S. D. Cruz, L. Sharma, *JAMA* **2020**, *323*, 1092. b) P. Zhou, H. Fan, T. Lan, X. L. Yang, W. F. Shi, W. Zhang, Y. Zhu, Y. W. Zhang, Q. M. Xie, S. Mani, X. S. Zheng, *Nature* **2020**, *556*, 255. c) D. Benvenuto, M. Giovanetti, A. Ciccozzi, S. Spoto, S. Angeletti, M. Ciccozzi, *J. Med. Vir.* **2020**, *92*(4), 455.

[24] S. A. Al-Jibori, A. S. Al-Janabi, S. Basak-Modi, S. S. Mohamed, H. Schmidt, *Trans. Met. Chem.* **2015**, *40*, 917.

[25] S. A. Al-Jibori, A. R. Al-Jibori, H. A. Mohamad, A. S. M. Al-Janabi, C. Wagner, G. Hogarth, *Inorg. Chim. Acta* **2019**, *488*, 152.

[26] S. A. Al-Jibori, S. H. Ali, A. S. Al-Janabi, C. Wagner, G. Hogarth, *Dalton Trans.* **2019**, *48*, 5520.

[27] O. A. Y. Al-Samrai, A. S. M. Al-Janabi, E. A. Othman, *Tikrit J. Pure Sci.* **2019**, *24*(5), 10. https://doi.org/10.25130/tjps.24.2019.083.

[28] M. E. A. Al-Doori, A. S. M. Al-Janabi, *Tikrit J. Pure Sci.* **2019**, *24*(5), 31. https://doi.org/10.25130/tjps.24.2019.086.

[29] R. A. Ammar, A. M. A. Alaghaz, A. S. Alturiqi, *Appl. Organomet. Chem.* **2018**, *32*, e4361. https://doi.org/10.1002/aoc.4361.

[30] A. M. A. Alaghaz, Y. A. Ammar, H. A. Bayoumi, S. S. A. Aldhlmani, *J. Mol. Struct.* **2013**, *1035*, 383.

[31] A. M. A. Alaghaz, *J. Mol. Struct.* **2014**, *1072*, 103.

[32] A. M. A. Alaghaz, Y. A. Ammar, H. A. Bayoumi, S. S. A. Aldhlmani, *J. Mol. Struct.* **2014**, *1074*, 359.

[33] B. Moulder, W. Lewert, R. M. Rippon, *Textbook of Microbiology*, 19th ed., Sannders, W.B. Comp. Ltd, Philadelphia, PA **1969**, p. 211.

[34] *Molecular Operating Environment (MOE), 2019.01*, Chemical Computing Group ULC, Montreal, QC, Canada **2021**.

SUPPORTING INFORMATION

Additional supporting information may be found online in the Supporting Information section at the end of this article.